Ultrafast laser ablation of graphite

M. Lenner,[1,*] A. Kaplan,[2] Ch. Huchon,[2] and R. E. Palmer[2]
[1]*Research Institute for Solid-State Physics and Optics, The Hungarian Academy of Sciences, H-1121 Budapest, Konkoly-Thege M. út 29-33, Hungary*
[2]*Nanoscale Physics Research Laboratory, School of Physics and Astronomy, University of Birmingham, Birmingham B15 2TT, United Kingdom*
(Received 25 December 2008; revised manuscript received 25 March 2009; published 7 May 2009)

We have studied single-shot femtosecond laser ablation of graphite by combining a variety of experimental techniques including Raman spectroscopy, atomic force microscopy as well as time of flight spectrometry. The comprehensive analysis reveals insights into the ablation process by exploring the surface structure, the fluence dependence, and the structural dynamics of the detachment. The results show formation and detachment of charged carbon products (such as graphene nanoflakes) from the surface. Time-resolved measurements of ion yields and velocities reveal strong quenching and revival of Coulomb explosion as a function of delay time in the range of 100–200 fs, suggesting a displacive motion between the topmost surface layers which regulates the optical properties of the system.

DOI: 10.1103/PhysRevB.79.184105 PACS number(s): 78.47.jc, 42.65.Re, 68.43.Tj, 81.05.Uw

I. INTRODUCTION

The properties of graphite materials (such as graphene, fullerenes, diamondlike carbon, and carbon nanotubes) have a key importance both in nanoscience and nanotechnology. For example, electric field effects in graphene[1] may open up the way to a new generation of electronic devices where the electronic properties of the material are controlled via external electric fields. In addition, the promising mechanical,[2] thermal,[3] and electronic properties[4,5] of carbon nanotubes have still not been fully characterized and exploited by research and industry.[6,7] Femtosecond laser ablation of graphite[8,9] offers a way to generate many of these carbon species.[10] Photoablation of graphite has been the focus of numerous studies so far: e.g., time-resolved measurements of surface reflectivity[8,11] shedded light on the transient change in the electronic properties of graphite after photoexcitation. It has been shown that electron-lattice temperature equilibration is possible at the picosecond time scale, before the onset of the hydrodynamic expansion that leads to disorder of the lattice and distortion of the optical properties. Amoruso *et al.*[9] investigated the optical emission of carbon nanoclusters produced by femtosecond laser ablation and estimated their temperature and size distribution, while Bae and Claeyssens *et al.*[12,13] analyzed the expansion of the ablation plume. The velocity distributions of single and double-charged atomic carbon cations delivered experimental evidence for nanoscopic Coulomb explosion during laser ablation as a consequence of effective localization of the surface charge,[14] whereas *ex situ* Raman spectroscopy measurements[15,16] and scanning electron microscopy (SEM) (Ref. 17) revealed information about crater formation and demonstrated the presence of an amorphous carbon layer over the damage spots.

In the present study we have applied a combination of different techniques to characterize the femtosecond laser ablation process both in time and space. First, we present a surface analysis that was aimed at determining the thickness and the reconstruction of the topmost nanocrystalline graphite layers remaining on the surface after single-shot laser ablation by applying a combination of micro-Raman spectroscopy and atomic force microscopy (AFM). The results reveal generation of graphite nanoparticles that reconstruct in a thin surface layer. The size and the orientation of the particles depend strongly on the laser fluence—when the laser fluence is decreased close to the damage threshold ($\sim$100 mJ/cm^2) the size of the particles increases up to a few tens of Angströms.

This phenomenon is well observable also in the size distribution of charged clusters, which is discussed in the Sec. II. Here, we characterize the fluence dependence of the positive-ion emission by means of time of flight (ToF) spectrometry, and correlate the results with the surface analysis. At fluences near the damage threshold we observe a significant amount of ions that consist of a few hundred carbon atoms (up to 550). The mass distribution shifts toward "lighter" fragments when the laser fluence increases and the "heavy" particles completely disappear from the mass spectrum at laser fluences above 700 mJ/cm^2. Although we use the term "fragment" throughout the paper, we shall emphasize that surface processes constitute the main focus of this study—fragmentation is not the direct scope of this paper. The detection of the emitted particles both on the surface (by means of AFM and Raman spectroscopy) and away from the surface (by means of ToF spectrometry) suggests a detachment—recapture dynamics during the laser ablation of graphite.

This process has been studied in the Sec. III where we investigate the dynamic detachment of ionic carbon products that can consist of graphene from graphite and its optical response in a highly nonequilibrium state through time-resolved spectroscopy and propose a qualitative argument to explain the experimental observations. We also estimate the decay time of the surface charge which sets a limit on Coulomb explosion and regulates the probability of a particle to be emitted from, or recaptured by, the surface.

II. EXPERIMENTAL

The details of the light source employed[18] are described elsewhere. The freshly cleaved graphite (highly oriented py-

rolitic graphite) samples were exposed to *p*-polarized Ti:sapphire laser pulses with 100 fs full width at half maximum (FWHM) duration centered at $\lambda_0=800$ nm at 19° incidence angle with respect to the surface normal under UHV conditions (background pressure $\approx 10^{-10}$ mbar). All experiments were single shot, i.e., each laser shot impinged on the target at a fresh site by rastering the sample and reducing the repetition rate of the laser system. The energy of the laser pulses was adjusted by inserting thin neutral density filters so that other pulse parameters (such as polarization and focal diameter) remained unchanged. Due to the relatively narrow laser spectrum ($\Delta\lambda \leq 10$ nm) the pulse duration was not significantly stretched by the insertion of the filters.

The ion spectra were recorded with a linear time of flight detector. The relatively small entrance aperture of the ion optics (∅ 3 mm) and the large distance to the sample (65 mm) ensured a reduced collection angle so that mainly straight ion trajectories were collected. Low dc electric fields in the extraction regime (≤ 40 V/cm) facilitated a low level of distortion in the acquired spectra and thus an energy resolution of ~0.1 eV for low-mass ions. On the other hand, these fields resulted in a limited energy resolution of a few eV on the high-mass end of the spectrum. The ions were detected with a microchannel plate (MCP) detector (response time ~1.5 ns) of 1 in. diameter after having passed a field-free drift tube of 1 m length. No post acceleration was used. The electric signals of the MCP were recorded with a multichannel scaler with a time resolution of up to 250 ps. The collection efficiency of the instrument was mainly determined by the response function of the MCP, which showed a gentle decrease toward higher masses but remained within the same order of magnitude in the particular mass ranges studied in this work.

The Raman measurements (Sec. I) were performed at Ar^+ wavelength ($\lambda_0=514.5$ nm). The illumination laser power was 1 mW, and the spot was focused to a diameter of ~1 μm. A collection time of 1.75 s per experimental point was used. The reference spectrum from bare graphite was recorded away from the damaged area. For the surface characterization we used a commercial AFM microscope operated in tapping mode. We have applied sharp Si tips with approximately 10 nm radius of curvature. Other experimental conditions can be found in Ref. 14.

In the time-resolved measurements (Sec. III) a pair of pulses was generated by attenuating the pulse energy to 3.75 and 1 μJ, respectively, and loosely focused onto the target with an $f=300$ mm lens. The energy of the weaker pulse was chosen to be slightly below the ion emission threshold.[14] The sample was rastered so that each site received a single pair of pulses. Each point represented in this section is an average over at least 60 single shots.

III. RESULTS AND DISCUSSION

A. Surface analysis

The single-shot damage spots generated with the laser system were subjected to *ex situ* surface analysis in order to characterize the impact of laser irradiation on the surface. As the first step, we performed a micro-Raman analysis on the damage spots that were created at average laser fluences, $\langle F\rangle$, of 160, 720, and 1200 mJ/cm^2. Some of the representative Raman spectra recorded at various locations, x, with respect to the spot centers are shown in Fig. 1. The spectra can be decomposed into three bands centered at 1360, 1575 and 1600 cm^{-1}. The sharpest band, at 1575 cm^{-1}, is attributed to the Raman active, $k=0$, E_{2g} mode.[19] The two other bands correspond to high-density phonons that are not active in the Raman spectra of the bulk material, but become observable due to symmetry breakdown in crystallites of a finite size as found in a disordered system.[20]

It has been demonstrated previously that the size of the nanocrystals formed on the graphite surface[19] and the thickness of the damaged layer[15] can be retrieved from the relative intensities of these bands. To calculate the depth, d_n, of the nanocrystalline layer we applied a procedure proposed by Dallas *et al.*[15] This method is based on the fact that the sharpest Raman peak of the graphite (1575 cm^{-1}) is attenuated by the overlayer of graphite nanocrystals. Thus, the ratio between the peak intensities recorded at pristine and damaged surface sites reveals information about the thickness of the overlayer. The observed Raman signal can be expressed as

$$I_{1575} \propto e^{-2\alpha_n d_n} \int_{d_n}^{\infty} e^{-2\alpha_G z} dz, \tag{1}$$

where $\alpha_n=581$ Å^{-1} and $\alpha_G=289$ Å^{-1} are the inverse optical penetration depths of glassy carbon and graphite, respectively, at the wavelength of $\lambda=514.5$ nm used for the Raman measurements.[21–23] Using Eq. (1), the depth of the damage can be estimated according to

$$d_n = -\frac{\ln(I_{1575}/I_{1575}^0)}{2(\alpha_n+\alpha_G)}, \tag{2}$$

where I_{1575}^0 is the Raman signal intensity of the pristine graphite measured outside the damaged area. We calculated d_n at different laser fluences and positions within the damage spots, as shown in Fig. 2(a).

The validity of the results and implications can be elucidated in the following way. Assuming linear absorption within the irradiated volume, one can suggest that at the depth $z=d_n(x)$ the energy density within the beam reaches the damage threshold (x being the transversal coordinate). Thus, at the damage depth, for a Gaussian beam, the ratio of the F amplitudes at $x=0$ and at any other x coordinate is unity and can be expressed as

$$\frac{F_{x=0,z_1}}{F_{x=x,z_2}} = \exp\left(-\frac{x^2+2\alpha_G\sigma^2(z_2-z_1)}{2\sigma^2}\right) = 1, \tag{3}$$

where σ is related to the FWHM of the laser beam profile as $2\sigma\sqrt{2\ln 2}$ and $(\alpha_G)^{-1}$ is taken to be 380 Å at 800 nm according to Ref. 22. z_1 corresponds to $d_n(x=0)$ at the center of the beam, and z_2 to the damage depth at $d_n(x=x)$. In this way, we can calculate values of σ at different irradiation fluences $\langle F\rangle$ by substituting z_1 and z_2 obtained from independent measurements,

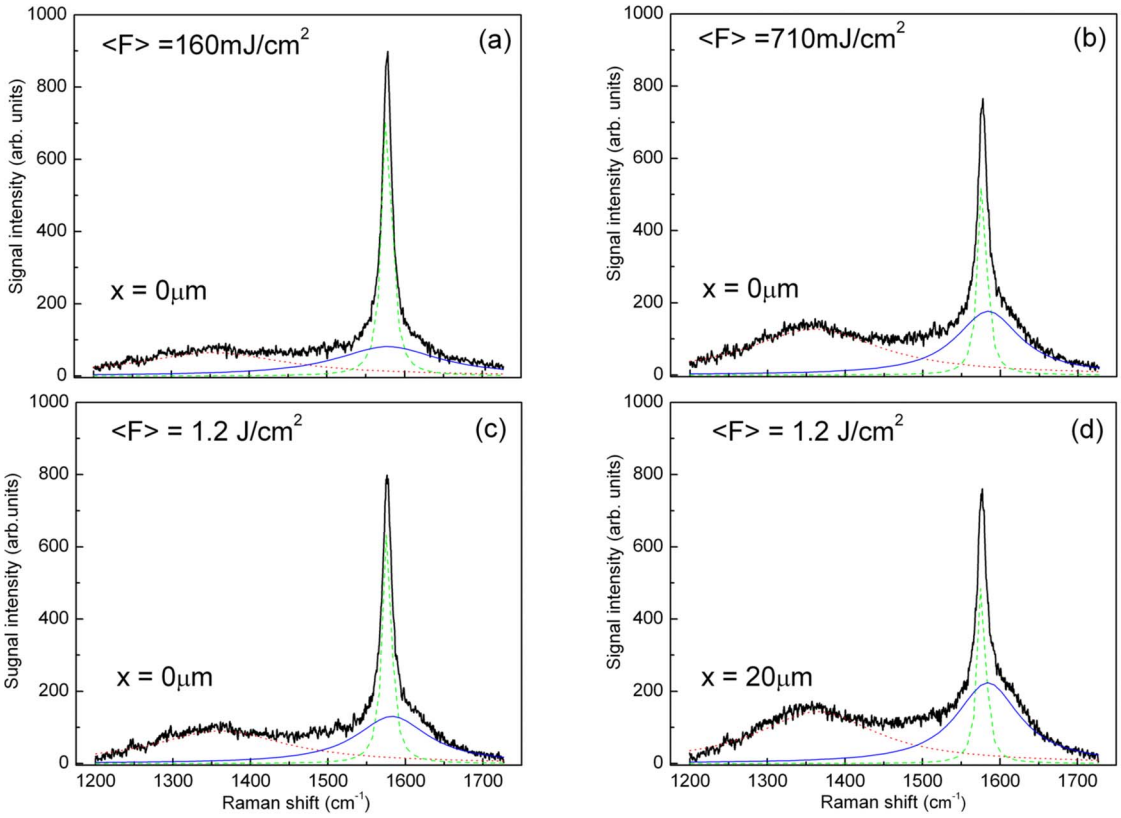

FIG. 1. (Color online) Some representative Raman spectra taken from the damage spots of the HOPG surface irradiated with single shot 100 fs laser pulses. The spectra were recorded at different laser fluences and different x positions with respect to the center of the damage spot. The black curve represents the raw data, the dotted red, dashed green, and solid blue lines correspond to the bands centered around 1360, 1575, and 1600 cm^{-1}, respectively.

$$|\sigma| = \frac{x}{\sqrt{2\alpha_G(z_1 - z_2)}}. \tag{4}$$

Now, in order to check the validity of the estimation, the calculated values of $|\sigma|$ can be compared to those obtained from the beam profile measurements (see Sec. II). For example, for $\langle F\rangle = 160$ mJ/cm^2 the calculated value of σ is 70 ± 30 μm and for $\langle F\rangle = 710$ mJ/cm^2 it is 48 ± 15 μm, reasonably close to the value obtained from the measured beam profile (~ 60 μm). No attempt to calculate this correlation has been done for $\langle F\rangle = 1.2$ J/cm^2, since $d_n(x)$ does not behave monotonically due to the contribution of additional processes that are not taken into account in this model, e.g., plasma generation,[24] cluster redeposition,[25] and shock

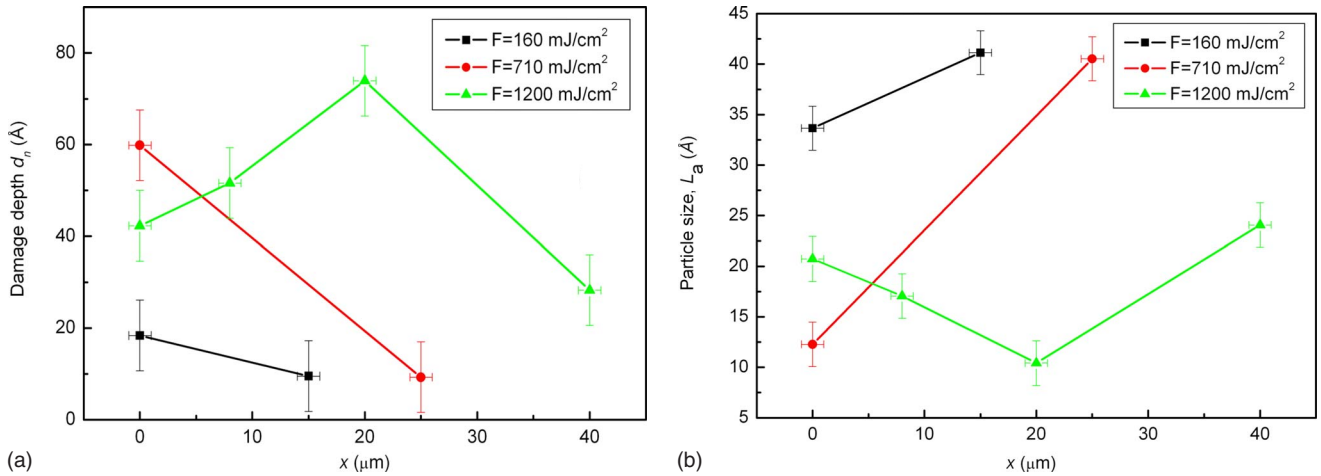

FIG. 2. (Color online) (a) Depth of the n-graphite layer evaluated from the integration of the 1575 cm^{-1} band on Fig. 1 using Eq. (2). (b) Size of the graphite nanoparticles obtained from the data displayed in Fig. 1 and the calibration curve from Ref. 19.

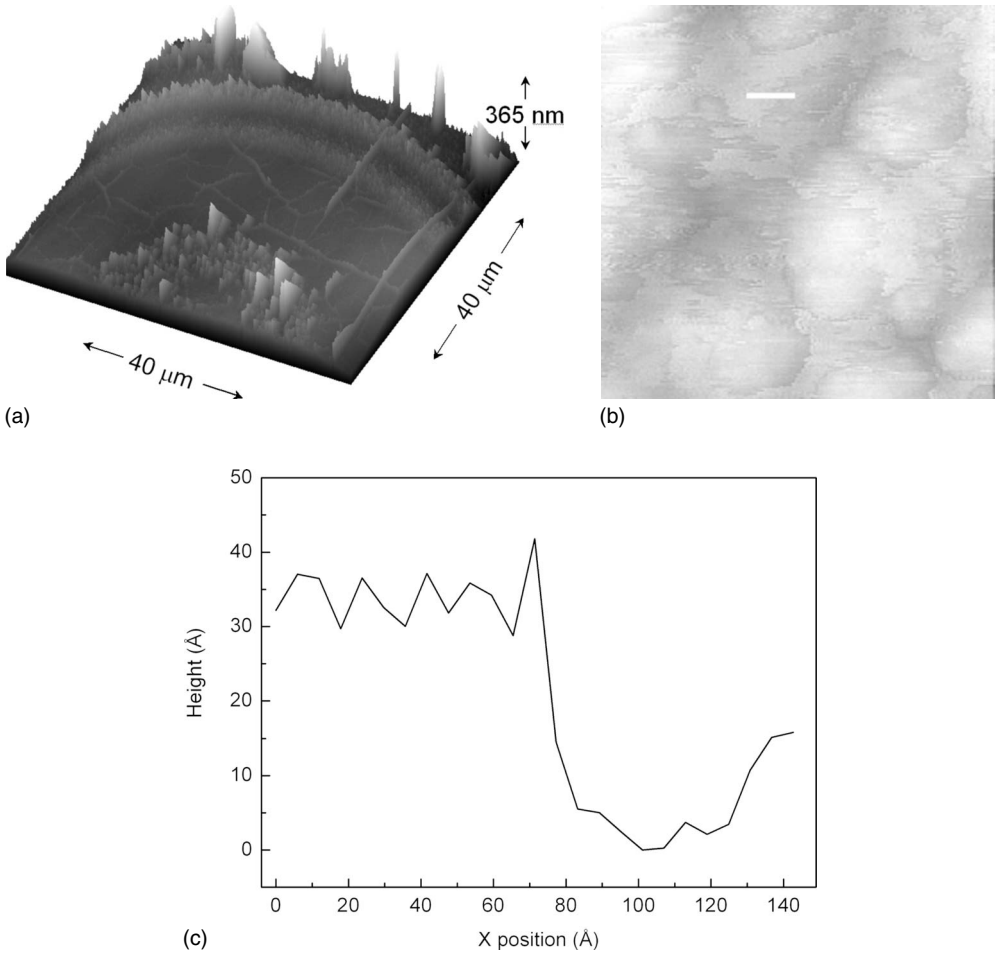

FIG. 3. (a) The AFM image (frame size 40×40 μm^2) of the damage spot generated at $F=1.2$ J/cm^2 laser fluence shows complex surface morphology. The different ablation areas (such as a small inner ring consisting of porous graphite, a flat plateau of an *n*-graphite layer with lines of up to 1 μm width and 10–15 nm height, and 3–5 μm wide outer rings) are highly visible. At the crater edges (not shown in this image) debris is deposited in a wide range of sizes from a few tens of nanometers up to a few microns. (b) Typical AFM image (frame size 125×125 nm) taken from the ablated HOPG surface at moderate laser fluences ($F\approx150$ mJ/cm^2). The depth profile (c) was extracted along the thick white line marked on the image (b). The height of the observed islands is consistent with the estimated diameter of the nanoparticles [see Fig. 2(b)].

waves,[26] which are reflected in the complex surface morphology shown in Fig. 3(a).

To be consistent with the applied method, we also tried to match the estimated damage depths at $\langle F_1\rangle=160$ mJ/cm^2 and $\langle F_2\rangle=710$ mJ/cm^2 at $x=0$. If the damage depth is governed by linear absorption, ignoring material removal due to the ablation, the relation

$$\alpha_G(d_{n2}-d_{n1})=-\ln\left(\frac{F_1}{F_2}\right) \tag{5}$$

has to be satisfied. Here, d_{n1} and d_{n2} are the thicknesses of the nanocrystalline graphite at fluences $\langle F_1\rangle$ and $\langle F_2\rangle$, respectively. If we now calculate, e.g., d_{n2} by substituting the thickness of the nanocrystalline graphite $d_{n1}=18$ Å [see Fig. 2(a)] and the corresponding fluence values into Eq. (5) we obtain 584 Å, which contrasts with the result we obtained using Eq. (2), as presented in Fig. 2(a). Such an apparent contradiction is most likely due to the fact that material removal was ignored in Eq. (5). This observation also suggests that at $\langle F_2\rangle=710$ mJ/cm^2 a layer of about 524 Å of graphite was removed while the rest [~60 Å, see Fig. 2(a)] resolidified into a layer of nanocrystalline material with a thickness profile proportional to the intensity distribution within the laser beam.

In order to gain further insight into the morphology of the ablated surface, we estimated the size of the nanocrystalline particles, L_a, using a generally accepted method described and applied elsewhere.[15,19,20,27] According to this method the ratio of the intensities of the disorder-induced Raman band (centered at 1360 cm^{-1}) to the band of the allowed Raman transition at 1575 cm^{-1}, (I_{1360}/I_{1575}) is inversely proportional to the average crystal size, L_a, within the damaged layer. Using the calibration curve provided in Ref. 19 and our Raman data we were able to estimate L_a at different locations of the damage spot, as plotted in Fig. 2(b). From this plot it is notable that there is a general tendency for the particle size to increase when the fluence decreases. This tendency is more distinct at lower fluences of 160 and 720 mJ/cm^2 when, as argued above, the redeposition pro-

cess is not strong. It is also worth mentioning that crystalline sizes at these fluences at certain locations (e.g., $x=15$ μm at $\langle F\rangle=160$ mJ/cm^2 and $x=25$ μm at $\langle F\rangle=710$ mJ/cm^2) coincide at $L_a\sim 40$ Å. This observation suggests that the absorbed energy at these points is similar, despite the fact that irradiation intensities fluences are different. To reconcile this contradiction we have to assume that ~500 Å of the graphite material has been ablated at $\langle F\rangle=710$ mJ/cm^2, as in the analysis of the damage depth. At this depth the local laser fluence at $x=25$ μm and $\langle F\rangle=710$ mJ/cm^2 reaches the same value as at $x=15$ μm and $\langle F\rangle=160$ mJ/cm^2. This suggests that most of the material is removed from the surface rather than resolidified and explains the absence of the diamondlike carbon (DLC) signatures present in the damaged layer after irradiation with nanosecond pulses.[28,29] In the case of femtosecond laser irradiation, material removal occurs at much faster time scales due to transient electrical fields[14,30] and/or dense electron-ion plasma acceleration[31] compared to the irradiation with "long" nanosecond pulses. Thus, it is likely that a significant fraction of excited graphite is emitted from the surface without undergoing phase transition.

In order to confirm the estimated size of the particles we took AFM images from the ablated surface with the highest possible lateral resolution, as shown in Fig. 3(b). The lateral resolution of the microscope did not allow us to resolve individual particles of 10–40 Å. However, the height of the structures could be resolved with subnanometer precision. We found that the height of the islandlike structures was consistent with the estimated diameter of the nanoparticles. This suggests that the nanocrystalline graphite nanoparticles are oriented randomly on the surface and can reconstruct in individual layers forming more-or-less contiguous islands of a few tens of nanometers lateral extent.

B. Fluence dependence

The first femtosecond ablation studies on the fluence dependence of the emission of neutral atoms and clusters from graphite were performed by Amoruso *et al.* by measuring the optical emission spectrum of atomic species, radicals, and clusters.[9] They reported a) a relatively low optical emission threshold for clusters which can be attributed to the ejection of large, intact fragments of the topmost layers of the graphite surface and b) a higher emission threshold for atoms and radicals which indicates bond breaking within the individual graphite layers during ablation. As for the atoms and radicals, the intensity of the light emission from the small fragments (i.e., atoms and radicals) shows a linear dependence as a function of the laser fluence.

We directly measured the yield of the emitted positively charged carbon clusters as a function of the time of flight at different incident laser fluences, as shown in Fig. 4. In order to describe the emission behavior of different clusters the ToF scale was divided arbitrarily into two regimes: (a) the "low mass" regime (labeled "LM" in Fig. 4) representing the clusters ranging from C_1^+ to C_{27}^+, and b) the "high mass" regime (labeled "HM" in Fig. 4) which corresponds to clusters from C_{30}^+ to C_{550}^+.

At the lowest fluence of 130 mJ/cm^2, emission peaks of positively charged carbon clusters are observable that are

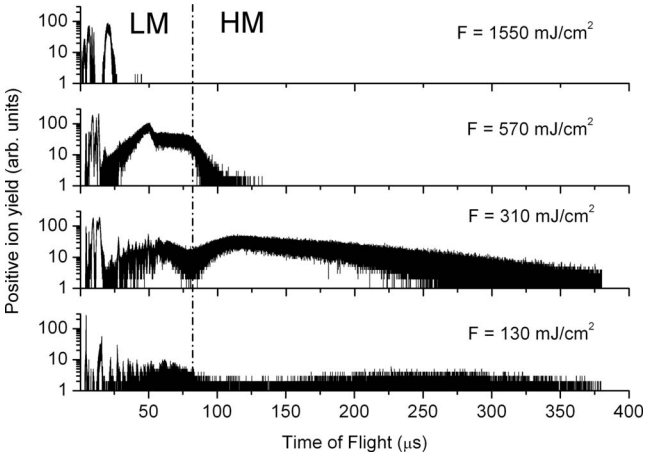

FIG. 4. Representative time of flight spectra of the positive ions recorded at different laser fluences. The labels "LM" and "HM" correspond to the low mass and the high mass regimes, respectively (see text).

well separated at the LM end and washed-out in the HM regime. This is due to the relatively low dc extraction field applied between sample and ion optics which was aimed at introducing a minimal distortion in the acquired spectrum. The yield of the positive ions generally increases with laser fluence up to about 310 mJ/cm^2 without significant change in the spectral shape in the LM range, where the peaks remain separated. At the same time, a substantial increase in the ion yield is observable for ToFs ranging from 90 to 250 μs (which corresponds to the range from C_{30}^+ to C_{240}^+). A further increase in the laser fluence ($F=570$ mJ/cm^2) leads to an unresolvable, smeared yield distribution in the LM range, and to a reduced yield in the HM regime, simultaneously. The smearing can be attributed to the fact that "LM" clusters are not created at a definite location in space (e.g., on the surface), but somewhere between the sample and the ToF entrance. Alternatively, an increasing spread of the ion velocities with increasing laser fluence may also explain this observation. At $F=1550$ mJ/cm^2 only small clusters are present in the spectrum and the HM signal completely disappears.

In order to further analyze the fluence dependence we carried out integration over both the ToF and the mass yields in the LM and HM regimes, as well as in the regime labeled "multiple charges," which includes all carbon atoms with higher charge states (C_1^{n+}, $n\geq 2$ corresponding to the ToF range from 6 to 11.3 μs) depicted in Fig. 5. The mass yields were derived from the ToF spectra by applying appropriate transformations. The mass yields were derived from the ToF spectra by applying appropriate transformations. This means that for the scale transformation (ToF to mass, for example) we performed a numerical trajectory simulation of the spectrometer using SIMION software. In order to obtain the mass (or velocity) distributions Jacobian transformation was applied. Integration over the ToF and the mass scale represents the total number of detected ions, and their corresponding mass, respectively.

Up to about 300 mJ/cm^2 the ion yields are nearly the same in both the "high" and "low" mass regimes, whereas

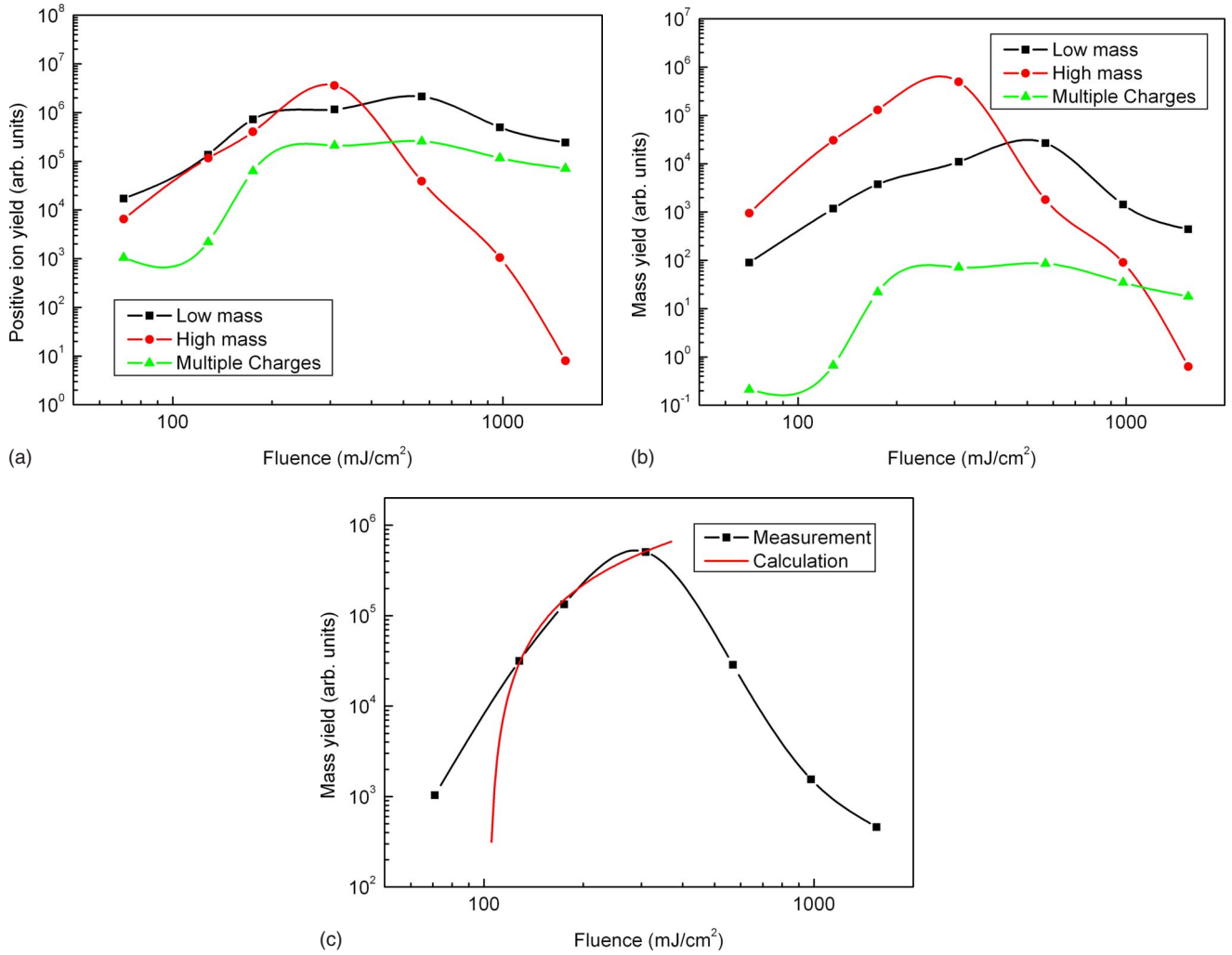

FIG. 5. (Color online) (a) Positive ion yield and (b) the removed ion mass as a function of laser fluence. The curves were obtained from the recorded ToF spectra by appropriate transformation (see text). (c) Measured (black line with squares) and calculated (red line) mass yield as a function of laser fluence. Scaling parameters are collection efficiency and ion detection threshold.

the mass yield in the high mass regime is higher by approximately 1 order of magnitude. In other words, the majority of the material removed leaves the surface in the form of heavy carbon products. This supports the theory of Jeschke *et al.*, which predicts removal of intact graphene sheets from the graphite surface during femtosecond laser ablation.[32] It is important to note that the cluster size estimated from the Raman measurements is about 40 Å at $F=160$ mJ/cm^2 (see Sec. I), which corresponds to $N\approx 500$ carbon atoms, assuming an in-plane atomic density of 4×10^{15} cm^{-2} (Ref. 14) and perfectly round particles. Such clusters are clearly observable in the ToF spectrum above ≈ 300 μs (Fig. 4). Because we can observe them both on the surface (AFM and Raman measurements) and at the ToF detector, we can conclude that ablation involves an emission-recapture dynamics, in which, initially emitted particles can either escape from or be recaptured by the surface. This mechanism is characterized and discussed in more detail in Sec. III C. In addition, the fact that the particles "survived" this relatively long flight time (of a few hundreds of microseconds) suggests that they are relatively "cold," i.e., below the critical temperature[33] of about 4600 K.

Above this fluence, the high mass signal drops strongly and finally disappears with increasing laser fluence and only small-size clusters are detected (see Fig. 4).

One way to explain this sudden disappearance of the heavy clusters may be to connect the observed phenomenon with the level of excitation on the surface. The carrier density n_e at a fluence $F=300$ mJ/cm^2 can be calculated[8] according to

$$n_e = \frac{(1-R)F\alpha}{h\nu}, \tag{6}$$

where the reflectivity is $R=0.3$,[11] and the absorption coefficient $\alpha^{-1}=380$ Å,[22] which gives $n_e=3\times 10^{23}$ cm^{-3}. It should be noted that the absorption coefficient is considered to be constant during laser excitation. Assuming that only π electrons are excited, comparison of the obtained carrier density with the atomic density in graphite (that is $n_a=1.76\times 10^{22}$ cm^{-3}) suggests that at this fluence level the entire π-system is excited. The above assumption is related to the band structure of graphite where optical absorption occurs primarily via the allowed π-π^* transitions around the

K point.[22,34] This high level of excitation leads to an instability of the graphene layers observed as an abrupt disappearance of the heavy clusters. This phenomenon bears a striking qualitative and quantitative resemblance to earlier predictions of Ref. 32, where, however, formation of ions was not taken into account. The above estimation also suggests that at even higher fluences the excitation energy is transformed into the breakage of in-plane bonds within the topmost graphene layers, which is reflected in the disappearance of the HM signal. The question, however, of whether the "small" positive cluster ions are generated at sufficiently high fluences (a) directly from the surface, or (b) during the flight to the detector by thermal disintegration of heavy clusters, remains open. It is likely that both processes are present during the ablation process.

In contrast to the results presented here, multishot measurements[35] show a different behavior, where the intensity of the heavy clusters saturates at high laser fluences. This could be ascribed to the fact that in the latter case the surface is "prepared" by subsequent laser pulses and redeposited clusters and debris are loosely bound to the surface. The optical absorption of these large particles is generally lower[36] than that of pristine graphite. Therefore, we can assume that heavy clusters are emitted from the crater edges, where the deposited energy is high enough for detachment without destroying them [see also the Raman measurement at 710 $\mathrm{mJ/cm^2}$ and also Fig. 2(b) in Sec. III A].

It is important to note that the emission of multiply charged ions (Fig. 5) at fluences as low as 70 $\mathrm{mJ/cm^2}$ can be regarded as a direct indication of the presence of nonthermal processes, given that thermal ionization at these low irradiation levels is impossible. Furthermore, the saturation of the signal sets in around the same laser fluence as the disappearance of the heavy clusters. These observations suggest that multiply charged clusters are not directly generated from the disintegration of heavy clusters (otherwise one would expect an increase in the yield of multiply charged clusters).

Below $F=310$ $\mathrm{mJ/cm^2}$ (where the heavy clusters are present) we can estimate the ablated volume as a function of the laser fluence based on a simple model that assumes Gaussian intensity distribution of the laser beam, linear absorption, and laser intensity-independent collection efficiency of the ions. In this case, the diameter of the ablation crater D_0 at depth z can be described by

$$D_0(z,F_0) = \sigma\sqrt{\ln\left(\frac{F_0\exp(-\alpha z)}{F_{tr}}\right)}, \tag{7}$$

where σ represents the beam waist and F_0 and F_{tr} are the peak laser fluence and the threshold fluence of the ion emission, respectively. To calculate the ablated volume one needs to evaluate the volume integral,

$$V(F_0) = \int_{z=0}^{z=z_{\max}} \left(\frac{D_0(z,F_0)}{2}\right)^2 \pi dz \tag{8}$$

with $z_{\max}$ being the maximum depth of the ablation crater, that is

$$z_{\max} = \frac{1}{\alpha}\ln\left(\frac{F_0}{F_{tr}}\right). \tag{9}$$

We compared the calculated results with the measurement in Fig. 5(c) by having the ion detection threshold and the collection efficiency as scaling parameters. One can obtain a reasonable fit in the fluence regime of $130\ \mathrm{mJ/cm^2} < F < 300\ \mathrm{mJ/cm^2}$, suggesting that the measured ion mass yield can be directly related to the ablated volume. Above the damage threshold, the change in the surface optical properties may lead to a suppression of the total amount of the absorbed energy,[11] which results in a lower ion yield. This could explain the discrepancy between the measured and the calculated curves at higher fluences. Alternatively, it is possible that positively charged clusters in the high mass regime may disintegrate rapidly near the surface into smaller fragments, including those neutral and negative charge states, which cannot be detected with the configuration used.

Despite the relatively good agreement at fluences close to the damage threshold, it is important to note that the above calculation can be considered as a very rough estimation only, which is based on several assumptions and simplifications (e.g., it excludes any ionization process).

C. Time-resolved dynamics

In this section we investigate the dynamic detachment of ionic carbon products that can include graphene from graphite and its optical response in a highly nonequilibrium state through time-resolved spectroscopy. The laser-induced detachment of intact graphene sheets from graphite has recently been both predicted[32] and demonstrated.[14]

The photoexcitation of graphite followed by the emission of charged particles can be described by a number of scenarios. One of these possible mechanisms is surface charging in the topmost layers of graphite upon strong laser excitation. The resulting impulsive electrostatic field can induce a displacive motion of the graphene sheets within graphite, which will be determined mainly by the interplay between the repulsive Coulomb force and the restoring van der Waals (VdW) force. Alternative explanations for the expansion of the topmost layers include (i) electronic repulsion,[32] (ii) electronic excitation of interlayer vibrational modes,[37] (iii) ultrafast melting,[8,38] or (iv) optical excitation of strongly coupled lattice vibrations.[39] It is important to note that (iii) involves both interlayer and in-plane phonon modes whereas (iv) is explained predominantly in terms of lateral vibrations. To identify the mechanism that is dominant in inducing the interlayer motion is out of the scope of our study.

In this section we attempt to interpret the experimental findings of the time-resolved measurements by a qualitative model based on the induced motion of the uppermost atomic layers leading to the detachment of i.a. graphene flakes from graphite. We propose that this approach can be considered as an alternative technique to time-resolved electron crystallography,[40] aiming to observe signatures of ultrafast structural changes in the graphite lattice. In our study, we utilized Coulomb explosion (CE) to track the structural dy-

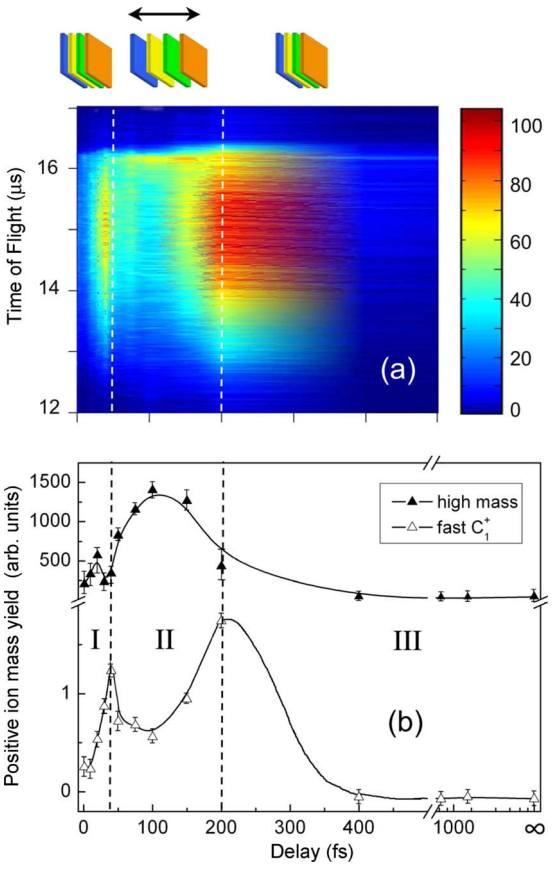

FIG. 6. (Color online) (a) Contour plot representation of the single-shot time of flight spectra of C_1^+ ions from graphite as a function of delay time. The false color scale represents the ion intensity (normalized to 100). (b) Particular ion yields as a function of delay time. High mass represents the integrated positive-ion yield detected in the mass range from C_{50}^+ to C_{1000}^+. "Infinite" delay represents the background signal, i.e., when only pump pulses impinge on the target. Solid lines serve to guide the eyes. At the top we show schematically the compression and expansion of the top graphene layers.

namics of a solid surface, specifically the detachment process of graphene flakes from graphite. In addition to the conventional CE imaging techniques, the interlayer motion can also be tracked by monitoring the CE efficiency rather than by measuring the kinetic energies of the ionic products. We believe that the utilized technique is applicable to the tracking of the interlayer motion regardless of which generation mechanism induced the motion.

The laser intensity is set such that the stronger beam (pump) initiates a displacive motion of the layers,[14] but the detachment of positive ions is minimized. The weaker (desorption) beam is adjusted to generate CE when it is temporally overlapped with the pump ($F_{\text{pump}}=150$ mJ/cm^2, $F_{\text{desorption}}=40$ mJ/cm^2, see also Fig. 5 in Sec. II). Thus, one can track the efficiency of the CE process as a function of pump-desorption delay time, which will be directly connected to the structure of the sample later in this section.

The experiments performed were aimed at shedding light on the temporal evolution of the detachment of highly excited graphene layers and their decomposition products, detected as carbon clusters of different sizes. Thus we measured the ToF spectrum of the products as a function of pump-desorption delay time. Figure 6(a) displays a contour plot of the ToF spectra of C_1^+ obtained at delay times up to 500 fs. Figure 6(b) plots the ion yield in two different mass ranges, "fast" C_1^+ only (which represents the integrated yield in the ToF range of 12–15 μs, i.e., kinetic energies of about 30–180 eV) and the integrated yield for masses ranging from C_{50}^+ to C_{1000}^+ (labeled as high mass).

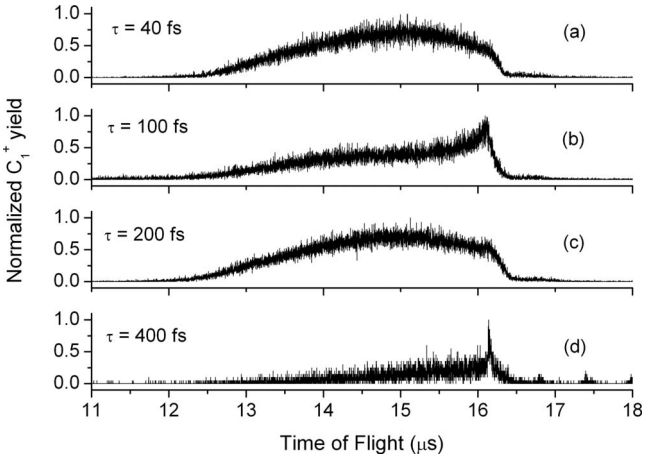

FIG. 7. Single-shot time of flight spectra of C_1^+ ions at different delay times. Data extracted from Fig. 6(a).

The very high kinetic energies suggest that the fast C_1^+ ions originate from CE. We therefore focused our attention on fast C_1^+ since its yield and velocity distribution serve as an indicator of the efficiency of the CE process. Figure 7 shows ToF spectra extracted from Fig. 6(a) for a representative sample of delay times.

The mass resolution of the spectrometer in the high mass regime is quite modest and does not allow the reliable reconstruction of the mass and velocity distribution of individual carbon species. Nevertheless, the yield information gained via integration over this mass range is sufficient to make a useful comparison between the behavior of the C_1^+ generated in CE and high-mass products originating from the detachment of ionic carbon products that can include intact graphene flakes.

In the first 40 fs [range I in Fig. 6(b)] the C_1^+ yield initially increases and the high-mass yield is nearly constant as a function of delay time, consistent with increasing CE efficiency. The transient enhancement of the C_1^+ yield (and thus the CE efficiency) can be attributed to the increased absorption of the surface due to the excitation of the saturated electron-hole plasma and the absorption of the free carriers on the leading edge of the pump pulse. The corresponding ToF spectrum [Fig. 7(a)] reveals intense emission of fast C_1^+ ions, suggesting that CE is the main (positive) ion generation mechanism in this regime,[30] as confirmed by the velocities of C_1^+ and C_1^{2+} ions, see below. However, in the range 40 fs$<\tau<$200 fs [range II in Fig. 6(b)] an "antiphase" behavior is observed, i.e., the yield of the fast C_1^+ ions decreases while the high-mass yield increases. At the same time, the ToF spectra show [Fig. 7(b)] a replacement of fast C_1^+ ions with slower C_1^+ ions with nearly thermal velocities

arriving at the detector at ~16.2 μs, indicating suppression of CE. What can explain such surprising behavior?

We propose that the observed antiphase behavior can be explained in terms of the dependence of the ionization probability (and consequently the CE efficiency) on the interlayer distance between the graphene sheets. Density-functional theory (DFT) calculations by Marinopoulos *et al.*[23] predict a very strong dependence of the optical absorption of graphite on the interlayer distance. For *p* polarization, the optical transitions are quenched with increasing interlayer separation and for *s* polarization the π-π^* transitions are "blocked" in the photon energy range of 0–10 eV. This weakening of the oscillator strength is also consistent with the predictions of a model based on the dipole selection rules for an isolated graphene layer.[41]

As a consequence of the suppressed optical absorption with increasing interlayer distance, the observed higher intensity (i.e., higher survival probability) of the heavy carbon products can be explained by less efficient dissociative ionization at the high-mass end of the spectrum. At the same time, the intensity of the C_1^+ signal decreases since the majority of the C_1^+ ions originates from the dissociation of the emitted heavy clusters via CE. Because of the high nonlinearity of the ion emission process (Fig. 5 in Sec. II), a relatively small decrease in the absorbed energy can lead to a significant suppression of the CE process, reflected in less efficient C_1^+ emission.

After reaching the "turning" point of the motion, where the repulsive force is equalized by the interlayer cohesive attraction, a fraction of the flakes can be recaptured and the interlayer distance starts to decrease, giving rise to more efficient absorption of the weaker desorption pulses again. This accounts for the "revival" of the emission of fast C_1^+ in Fig. 6(b), which begins at ≈100 fs and reaches another maximum at around 200 fs delay time [see also Fig. 7(c)]. Over the same delay time range the heavy mass signal drops again, indicating strong dissociative ionization due to the more efficient optical absorption.

For pump-desorption delay times of >250 fs [range III in Fig. 6(b)], the ion yields decrease for both ion mass regimes. At the same time, the fast C_1^+ ions disappear from the ToF spectrum and only very low kinetic energy C_1^+ ions are observable [Fig. 7(d)], which can be explained by the decay of the excitation energy and the consequent termination of the CE process. The "pump only" contribution (background signal) is displayed at "infinite" delay time in Fig. 6(b).

To estimate the decay time τ of the electrostatic field induced by the pump excitation we studied the velocity distributions and the momentum ratios of the emitted C_1^+ and C_1^{2+} ions, which were obtained by direct transformation of the ToF spectra.

Figure 8 shows the momentum ratios, while the inset displays the mean velocities of the corresponding ions themselves, in both cases as a function of delay time. Up to ≈200 fs the momentum ratio is close to a value of 2 suggesting that the momentum of the emitted ions scales with their charge state.[30,42] This behavior functions as an indication of the existence of an impulsive electrical field induced by the combination of the pump and the desorption pulses, so that we can estimate the charge decay time τ of 200 fs.[43]

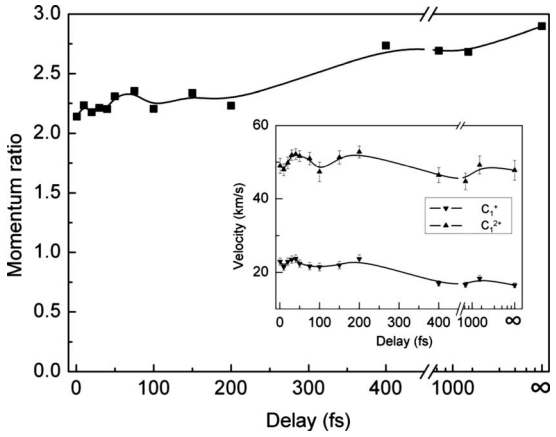

FIG. 8. Momentum ratio for the emitted C_1^+ and C_1^{2+} ions as a function of delay time. The inset displays the mean ion velocities obtained from the time of flight spectra. Infinite delay time represents the background signal, i.e., when only pump pulses are applied to the target.

Because the proposed technique for tracking the interlayer dynamics in graphite is based on the efficiency of the CE process, the decay of the surface charge sets an upper time limit for its applicability. It is, however, able to provide signatures of the femtosecond dynamics of the laser-induced nuclear motion.[44]

IV. SUMMARY

In summary, we combined different experimental techniques in order to characterize single-shot femtosecond laser ablation of the graphite surface. *Ex situ* micro-Raman spectroscopy measurements revealed the thickness of the *n*-graphite layer and the size of the nanocrystals that were formed at different laser fluences. We showed that the thickness of the nanocrystalline layer remaining on the surface of the ablation crater depends on the *locally* deposited energy (i.e., the energy density) and amounts to a few nanometers. This layer consists of small nanoclusters with particle sizes ranging from 10–40 Å. From the AFM analysis we concluded that these particles form islands of a few tens of nanometers in lateral dimensions on the surface. Moreover, the complex surface morphology appearing around $F = 1.2$ mJ/cm^2 suggests that a multitude of different phenomena (including e.g., thermodynamical expansion, shock wave formation, surface recapture of clusters and recrystallization) take place in the crater formation at moderately high fluences.

Time of flight spectroscopy allowed the direct characterization of the ionic products generated upon laser irradiation. At lower laser fluences (up to ~300 mJ/cm^2) a strongly nonlinear increase can be observed with increasing laser fluence, where the majority of the carbon ions is removed in the form of heavy carbon products (most likely graphene sheets). Above this fluence, the positive-ion signal decreases and the majority of the detected carbon species is found exclusively in the low-mass end of the spectrum, i.e., clusters are smaller than C_4^+. In addition, there is no clear separation between

individual mass channels. The high level of the excitation of the π-system supports the idea of bond breaking within the graphene planes which leads to the formation of small clusters.

Time-resolved measurements of the CE efficiency offered an alternative means to track the lattice dynamics of solid surfaces *in situ*. The method was employed to study the motion of the topmost graphene layers of graphite. A displacement of the layers, driven by the competition between laser-induced repulsive and intrinsic attractive forces, is manifested in a corresponding shift of the center of gravity of the velocity spectrum of the emitted ions, which provides a novel indicator for tracking the surface dynamics. The decay of the transient surface charge (within about 200 fs) sets a limit to the application of the method proposed. It suggests however, that detachment of graphene is possible via nonthermal pathways, within a few hundred femtoseconds. We argue that the proposed method is generally applicable to the study of the lattice dynamics of a manifold of materials where CE is possible. In addition, we propose that metastable free-standing graphene can be generated and studied by femtosecond laser pulses, its transient optical properties can be characterized, and its transformation dynamics into stable structures (e.g., fullerenes and carbon nanotubes) can be tracked.

ACKNOWLEDGMENTS

We wish to acknowledge the help of E. Kolodney (Technion, Israel) with the Raman measurements. We thank the EPSRC and the European Union "XTRA" Research Training Network for financial support of the work. M.L. was supported by the Marie Curie Intra-European Fellowship MEIF-CT-2006-024231 and the Marie Curie European Reintegration Grant MERG-CT-2007-204172.

*Corresponding author; FAX: +36-1-3922215; lenner@szfki.hu

[1] K. S. Novoselov, A. K. Geim, S. V. Morozov, D. Jiang, Y. Zhang, S. V. Dubonos, I. V. Grigorieva, and A. A. Firsov, Science **306**, 666 (2004).
[2] E. T. Thostenson, Z. F. Ren, and T. W. Chou, Compos. Sci. Technol. **61**, 1899 (2001).
[3] M. J. Biercuk, M. C. Llaguno, M. Radosavljevic, J. K. Hyun, A. T. Johnson, Appl. Phys. Lett. **80**, 2767 (2002).
[4] M. P. Anantram and F. Leonard, Rep. Prog. Phys. **69**, 507 (2006).
[5] A. Gambetta, C. Manzoni, E. Menna, M. Meneghetti, G. Cerullo, S. Tretiak, A. Piryatinski, A. Saxena, R. L. Martin, and A. R. Bishop, Nat. Phys. **2**, 515 (2006).
[6] A. H. Romero, M. E. Garcia, F. Valencia, H. Terrones, M. Terrones, and H. O. Jeschke, Nano Lett. **5**, 1361 (2005).
[7] A. Martinez, K. M. Zhou, I. Bennion, and S. Yamashita, Opt. Express **16**, 15425 (2008).
[8] D. H. Reitze, X. Wang, H. Ahn, and M. C. Downer, Phys. Rev. B **40**, 11986 (1989).
[9] S. Amoruso, G. Ausanio, M. Vitiello, and X. Wang, Appl. Phys. A. **81**, 981 (2005).
[10] S. Arepalli, W. A. Holmes, P. Nikolaev, V. G. Hadijev, and C. D. Scott, J. Nanosci. Nanotechnol. **4**, 762 (2004).
[11] D. H. Reitze, H. Ahn, and M. C. Downer, Phys. Rev. B **45**, 2677 (1992).
[12] C. H. Bae and S. M. Park, J. Chem. Phys. **117**, 5347 (2002).
[13] F. Claeyssens, S. J. Henley, and M. N. R. Ashfold, J. Appl. Phys. **94**, 2203 (2003).
[14] M. Lenner, A. Kaplan, and R. E. Palmer, Appl. Phys. Lett. **90**, 153119 (2007).
[15] T. Dallas, M. Holtz, H. Ahn, and M. C. Downer, Phys. Rev. B **49**, 796 (1994).
[16] Á. Mechler, P. Heszler, Zs. Márton, M. Kovács, T. Szörényi, and Zs. Bor, Appl. Surf. Sci. **154-155**, 22 (2000).
[17] M. D. Shirk and P. A. Molian, Carbon **39**, 1183 (2001).
[18] A. Kaplan, A. Sajwani, Z. Y. Li, R. E. Palmer, and J. P. Wilcoxon, Appl. Phys. Lett. **88**, 171105 (2006).
[19] F. Tuinstra and J. L. Koenig, J. Chem. Phys. **53**, 1126 (1970).
[20] B. S. Elman, G. Braunstein, M. S. Dresselhaus, G. Dresselhaus, T. Venkatesan, and J. M. Gibson, Phys. Rev. B **29**, 4703 (1984).
[21] M. Williams and E. Arakawa, J. Appl. Phys. **43**, 3460 (1972).
[22] E. A. Taft and H. R. Philipp, Phys. Rev. **138**, A197 (1965).
[23] A. G. Marinopoulos, L. Reining, A. Rubio, and V. Olevano, Phys. Rev. B **69**, 245419 (2004).
[24] S. Amoruso, G. Ausanio, A. C. Barone, R. Bruzzese, L. Gragnaniello, M. Vitiello, and X. Wang, J. Phys. B **38**, L329 (2005).
[25] E. A. Stach, V. Radmilovic, D. Deshpande, A. Malshe, D. Alexander, and D. Doerr, Appl. Phys. Lett. **83**, 4420 (2003).
[26] N. M. Bulgakova, I. M. Bourakov, and N. A. Bulgakova, Phys. Rev. E **63**, 046311 (2001).
[27] T. C. Chieu, M. S. Dresselhaus, and M. Endo, Phys. Rev. B **26**, 5867 (1982).
[28] R. Windholz and P. A. Molian, J. Mater. Sci. **32**, 4295 (1997).
[29] Á. Mechler, P. Heszler, Z. Kántor, T. Szörényi, and Zs. Bor, Appl. Surf. Sci. **138-139**, 174 (1999).
[30] R. Stoian, A. Rosenfeld, D. Ashkenasi, I. V. Hertel, N. M. Bulgakova, and E. E. B. Campbell, Phys. Rev. Lett. **88**, 097603 (2002).
[31] N. M. Bulgakova, A. V. Bulgakov, and O. F. Bobrenok, Phys. Rev. E **62**, 5624 (2000).
[32] H. O. Jeschke, M. E. Garcia, and K. H. Bennemann, Phys. Rev. Lett. **87**, 015003 (2001).
[33] M. Togaya, Phys. Rev. Lett. **79**, 2474 (1997).
[34] G. S. Painter and D. E. Ellis, Phys. Rev. B **1**, 4747 (1970).
[35] A. Kaplan, M. Lenner, C. Huchon, and R. E. Palmer, Appl. Phys. A **92**, 999 (2008).
[36] N. Gioti and S. Logotheidis, Diamond Relat. Mater. **12**, 957 (2003).
[37] J. Maultzsch, S. Reich, C. Thomsen, H. Requardt, and P. Ordejon, Phys. Rev. Lett. **92**, 075501 (2004).
[38] S. I. Ashitkov, M. B. Agranat, P. S. Kondratenko, S. I. Anisimov, V. E. Fortov, V. V. Temnov, K. Sokolowski-Tinten, P. Zhou, D. von der Linde, JETP Lett. **75**, 87 (2002).
[39] T. Kampfrath, L. Perfetti, F. Schapper, C. Frischkorn, and M.

Wolf, Phys. Rev. Lett. **95**, 187403 (2005).
[40] F. Carbone, P. Baum, P. Rudolf, and A. H. Zewail, Phys. Rev. Lett. **100**, 035501 (2008).
[41] F. Bassani and G. Pastori Parravicini, Nuovo Cimento A **50**, 95 (1967).
[42] A. Kaplan, M. Lenner, and R. E. Palmer, Phys. Rev. B **76**, 073401 (2007).
[43] Note also, that the high mean ion velocities ($\approx$25 and $\approx$52 km/s for C_1^+ and C_1^{2+}, respectively) in the CE regimes (around 40 and 200 fs delay times) also suggest the presence of a strong impulsive electric field on the surface, which is generated primarily by the localized surface charge.
[44] P. Stampfli and K. H. Bennemann, Phys. Rev. B **49**, 7299 (1994).